



# In situ sounding of radiative flux profiles through the Arctic lower troposphere

Ralf Becker<sup>1</sup>  · Marion Maturilli<sup>2</sup> · Rolf Philipona<sup>3</sup> · Klaus Behrens<sup>1</sup>

Received: 1 November 2019 / Accepted: 22 April 2020 / Published online: 15 May 2020  
© The Author(s) 2020

## Abstract

In situ profiles and fixed-altitude time series of all four components of net radiation were obtained at Ny-Ålesund, Svalbard (78.9° N, 11.9° E), in the period May 04–21, 2015. Measurements were performed using adapted high-quality instrumentation classified as “secondary standard” carried by a tethered balloon system. Balloon-lifted measurements of albedo under clear-sky conditions demonstrate the local dependence on altitude and on the surface inhomogeneity of this parameter over coastal terrain of Ny-Ålesund. Depending on the surface composition within the sensor’s footprint near the coastline, the albedo over predominantly snow-covered surfaces was found to decrease to 0.548 and 0.452 at 494 m and 881 m altitude compared with 0.731 and 0.788 measured with near-surface references, respectively. Albedo profiles show an all-sky maximum at 150 m above surface level due to local surface inhomogeneity, and an averaged vertical change rate of  $-0.040/100$  up to 750 m aboveground level (clear sky) and  $-0.034/100$  m (overcast). Profiling of arctic low-level clouds reveals distinct vertical gradients in all radiative fluxes but longwave upward at the cloud top. Observed radiative cooling at the top of a partly dissolving stratus cloud with heating rates of  $-40.4$  to  $-62.1$   $\text{Kd}^{-1}$  in subsequent observations is exemplified.

**Keywords** Atmosphere · Arctic · In-situ profiling · Albedo · Clouds · Heating rates

---

✉ Ralf Becker  
Ralf.Becker@dwd.de

<sup>1</sup> Deutscher Wetterdienst, Meteorologisches Observatorium Lindenberg, Am Observatorium 12, 15848 Tauche, Germany

<sup>2</sup> Helmholtz-Centre for Polar and Marine Research, Alfred Wegener Institute, Telegrafenberg A45, 14473 Potsdam, Germany

<sup>3</sup> Federal Office of Meteorology and Climatology MeteoSuisse, Chemin de l’Aerologie, 1530 Payeme, Switzerland

## 1 Introduction

Solar incoming radiation, emitted terrestrial radiation, and the shortwave and longwave interactions in the atmosphere and at the Earth surface are the driving forces of our weather and climate. Particular importance for the Earth's energy budget is attributed to clouds, as they reflect incoming solar radiation back to space while trapping terrestrial radiation in the atmosphere (Ramanathan et al. 1989). Their actual radiative effect depends on the cloud temperature, phase, surface albedo, cloud microphysics, and sun elevation. Especially in the Arctic, where solar radiation with low elevation angles over the high albedo of snow and sea ice encounters low-level clouds, the cloud net radiative effect results in a warming of the surface through most of the year (Shupe and Intrieri 2004). Climate forcing-induced changes in cloudiness (Norris et al. 2016) may alter the atmospheric radiation budget. Recent studies relying on high-quality ground-based radiation network data revealed that shortwave downward radiation is subject to change through the decades (Wild 2012). Accurate observation of the components of the near-surface radiation budget is therefore an essential task (IPCC 2014). Such quality ground-based measurements are performed for example in the context of the Baseline Surface Radiation Network (BSRN; Ohmura et al. 1998; Driemel et al. 2018). The single components are quantified on a global scale based on satellite data of the Clouds and Earth's Radiant Energy System (CERES) at top-of-atmosphere (Trenberth et al. 2009).

To fully understand the radiative effects of clouds and other factors in the atmospheric column, the ground-based data quality standard needs to be expanded into the free atmosphere. Measurement equipment mounted on masts and towers at different heights are used to investigate fluxes in the lower range of the planetary boundary layer. For mid-latitude clear-sky and moderate wind conditions, the radiative flux divergence between 2 and 48 m above-ground tends to be largest in the early evening hours (Sun et al. 2003). To determine the radiative cooling at night, Steeneveld et al. (2010) analyzed net longwave radiation at several steps from 1.3 to 20 m aboveground and found typical longwave heating rates of  $-1.8 \text{ K h}^{-1}$  below 10 m and  $-0.5 \text{ K h}^{-1}$  between 10 and 20 m height, respectively. To expand the ground operation to higher altitudes, several balloon-borne platforms have been developed. The long history of meteorological in situ soundings by tethered balloons and kites reaches back to the late nineteenth century. A comprising review of early activities, developments, and technical fundamentals is provided in Dubois (1961) (in German). Duda et al. (1991) operated such a platform with standard meteorological instruments, longwave and shortwave radiation sensors, and a cloud droplet particle analyzer to determine microphysical and radiative properties of stratocumulus clouds in a marine boundary layer. They compared measured vertical radiative flux profiles with calculated fluxes. Even though correspondence was quite good in the longwave range, discrepancies in solar heating rates in the clouds appeared to be larger than expected. The lighter short- and longwave radiometer payload developed by Alzheimer et al. (1993) was properly levelled in flight by using accelerometers and a mechanical correction system. A system for in situ profiling of radiative fluxes through the entire troposphere up to the lower stratosphere was recently introduced by Philipona et al. (2012) and Kräuchi and Philipona (2016). Airborne measurements of the REFLEX I & II campaigns were used by Freese and Kottmeier (1998) to investigate the radiative fluxes between stratus clouds and marine surfaces including sea ice cover at very low sun elevations. Moving platforms need to apply a proper tilt correction to respective irradiance measurements, and the a priori knowledge of the relative contribution of the direct and diffuse components to the shortwave downward irradiance is of particular importance (Boers et al. 1998; Wendisch et al. 2001; Webb et al. 2004;

Long et al. 2010). A methodology for determining constant pitch and roll offsets and an applicable correction for tilts up to  $\pm 10^\circ$  was developed (Long et al. 2010).

Based on 17 aircraft flights through unbroken stratocumulus clouds off the Californian coast, Gerber et al. (2014) found cooling rates from 10 to 15  $\text{K h}^{-1}$  at the cloud top and furthermore identified a different behavior in the slow-response sensors between ascent and descent profiles. For subvisible cirrus clouds in the tropics, Bucholtz et al. (2010) determined a heating rate of 2.50–3.24  $\text{K d}^{-1}$ . Recently, Turner et al. (2018) calculated heating rate profiles based on a 2-year cloud microphysical property dataset obtained at the ARM site near Barrow, Alaska, finding the radiative heating of single-layer ice clouds being one order of magnitude lower compared with that of liquid-water clouds.

As the development of ground-based and satellite-based remote sensing techniques is evolving, a growing need for high-quality in situ validation data emerges. In terms of the radiative effect, the physical properties of clouds, atmosphere, and the underlying surface are key components of the climate system which rely on precise measurements.

The albedo is the most apparent surface property that is subject to seasonal changes in mid and high latitudes due to the growing cycle of vegetation and/or the variable snow and sea ice cover, respectively. It is defined as the ratio of upward and downward shortwave fluxes and is conventionally measured near the surface. For the Arctic site Ny-Ålesund, Svalbard, the snow melt in the beginning of summer is characterized by a sharp transition from high (0.8) to low (0.1) albedo values. In recent decades, a tendency toward an earlier onset of melting has been found (Maturilli et al. 2015).

With our study, we aim to initially describe the baseline clear-sky vertical radiative flux profiles for the Arctic location of Ny-Ålesund, Svalbard. We intend to quantify the role of the footprint size for albedo determination over this complex Arctic fjord environment, and provide a first observation of the vertical resolved radiative flux in the presence of clouds. This can be achieved using an irradiance observation package carried by a tethered balloon. The benefit of such systems is the availability of a full profile from surface to cloud top as well as the option to sense the same atmospheric column several times sequentially with a moderate speed of 2  $\text{ms}^{-1}$ . During the tethered balloon campaign at Ny-Ålesund, Svalbard, with 9 days of suitable weather conditions, a total of 32 profiles and two extended time series (2 h 20 m and 4 h 15 m) were recorded.

The paper is structured as follows: Section 2 is dedicated to the radiation sensors, the sounding setup, and the interpretation and correction of data. In section 3, the observations are presented. Here, one focus is set on land surface characterization with respect to the observation height under both clear sky and overcast conditions. The second focus is set on radiative flux profiling in the presence of clouds with the case study of a dissolving Arctic stratus cloud. Results on the comparison of the observations to simulated fluxes and cooling effects associated with cloud profiles are given in section 4. The outcome is summarized and potential further activities are indicated in section 5.

## 2 Instruments and methods

### 2.1 Radiation sensors and sounding setup

For the purpose of net radiation observations in the lower troposphere, a dedicated sonde was developed, consisting of two paired upward- and downward-looking shortwave and longwave

instruments, respectively. For the shortwave (solar) range, CMP22 pyranometers by Kipp & Zonen are applied for the sake of their reduced sensitivity to fast changes of ambient air temperature. Measurements of longwave (terrestrial) radiative flux densities are obtained with CGR4 pyrgeometers by Kipp & Zonen. Both, short- and longwave instruments are categorized as secondary standard; therefore, the selected sensors have a high quality that is achieved within a 3% margin to reference of 95% of the readings in hourly total and 2% in daily totals (WMO 2018). The measurement uncertainty for use under ambient conditions is given by the manufacturer and specified as 2% with CMP22 and 3% with CGR4 for daily totals (Kipp and Zonen 2001, 2004). Calibration is performed in the field in a yearly cycle at the Regional Radiation Center (WMO-RA VI) and National Radiation Center located at the Lindenberg Meteorological Observatory of Deutscher Wetterdienst and therefore linked to World Radiometric Reference (WRR) in the solar and to the World Infrared Standard Group (WISG) of pyrgeometers in the longwave region via the local standard groups, respectively. Tracking the calibration factors of all sensors before and after construction of the sonde revealed no distinct change in the characteristics of the sensor by means of altered factors. The instrument bodies were modified to allow the mounting as upward- and downward-oriented pairs. To save weight, no radiation shields were used. In general, hardware weight was saved wherever feasible to increase the free buoyancy. In contrast to near-surface observations, no ventilation was mounted assuming an adequate air stream present during all flights. The instruments were mounted and levelled on a glass fiber pole attached to a flexible holder and hooked to the tethered line. A wind vane on the back enables horizontal orientation of the sonde in the air stream. Figure 1 is showing the instrumentation. For the data acquisition, two commercial lightweight loggers manufactured by Driesen & Kern are used. In total, four loggers are needed to store signals, instrument temperatures, and pitch and roll angles.

The storage interval was set to 1 min (averages, no standard deviations) for slow-responding radiation sensors and roll and pitch angles, and to 1 s for the meteorological sensors. Probing the free atmosphere requires operating the equipment within the range of meteorological parameters proposed by the manufacturer. For both the CMP22 pyranometer

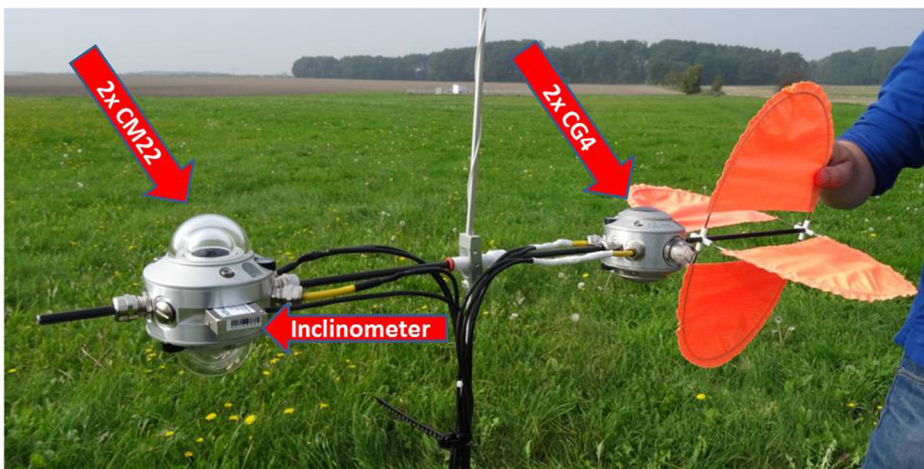


**Fig. 1** Instrumental setup of the net radiation sonde. A pair of CMP22 and a fixed mounted 2-axis inclinometer to the left, a pair of CGR4 plus wind vane on the right-hand side. A small box logger, housing the loggers, is mounted about 1.5 m below the sonde

and the CGR4 pyrgeometer, the range of low temperature sensitivity is given down to  $-20\text{ }^{\circ}\text{C}$ . Below  $-20\text{ }^{\circ}\text{C}$ , there is a higher instrument-specific temperature dependence of the signal, up to 5% according to the manufacturer. Another important number is the stability of the signal in case of strong temperature lapse rates. Usually, it is described that a gradient of  $5\text{ K h}^{-1}$  maximum will keep the so-called Zero-offset B below  $2\text{ W m}^{-2}$ , which is quite a low effect. On the other hand, the sonde was expected to face temperature gradients of  $5\text{--}10\text{ K h}^{-1}$  in flight. To minimize temperature adaption effects, the sensors were exposed to ambient conditions at least 30 min before ascent. Overall, the payload resulted in 2410 g including cables, plugs, loggers, and housing. Without a ventilation unit, no dedicated power supply for operating the radiometers is needed.

## 2.2 Tethered balloon system and auxiliary sensors

- The tethered balloon soundings at Ny-Ålesund, Svalbard, were conducted with an average ascent/descent rate of  $2\text{ ms}^{-1}$ , taking about half an hour to complete a vertical profile. Therefore, stable radiation conditions of either clear sky or stratified cloud cover were necessary to assure the recording of a steady vertical profile. The maximum sensing height was 2 km aboveground as preset by the local flight authority. The equipment allowed continuous measurements of several hours, and comprised a Vaisala TT12 tether sonde system including a streamlined tethered balloon of TTB329 series with a length of 5.2 m, a maximum diameter of 2.3 m, and a volume of  $9\text{ m}^3$ , made of 0.08-mm polyurethane
- An electrical winch TTW111 with automatic engine shutdown including about 2000-m tether line
- A DigiCora III MW21 receiving system comprising laptop, receiver, antenna, and the software. The use of the quite old software is due to the Vaisala tether sonde system which is only operational with according MW21 software.
- Several tethersondes of type TTS111 for in situ measurements of meteorological standard parameters

Wind, temperature, and humidity data were measured with 1-Hz time resolution and transferred to ground via telemetry. Temporal synchronization of the different sensors was not a critical issue since the radiation sensors had a slower response. The operation of the tethered balloon was restricted to meteorological conditions without precipitation. Low wind speed was required throughout the respective air column, with optimum conditions below  $5\text{ ms}^{-1}$  and endurable conditions up to  $10\text{ ms}^{-1}$ . The wind direction was retrieved by the position of the wind vane, using a magnetic compass that was corrected for the launch position. According to the magnetic declination map available at <http://geomag.nrcan.gc.ca> using the IGRF-12 model of 2015, the deviation of magnetic to geographic north is  $6^{\circ} 14.94'$ , toward east. As the accurate observation of wind direction was crucial for the correction of the tilt, we thoroughly compared the wind measurements by tether sonde with high-resolution wind profiles measured by Doppler wind lidar from the roof of the observatory building about 30 m horizontal distance from the launch site. The data were generally in good agreement with deviations smaller than  $10^{\circ}$ . We compared the tether sonde wind data with wind profiles by the local Doppler wind lidar which revealed an east-to-southeasterly flow at 900 m on May 8, 18–21 UTC, as well as at 500 m on May 13, 14–19 UTC. The data analysis has been limited to such conditions with low variability in wind direction.

Tilting of the sonde is a potential source of error, mainly regarding the shortwave downward flux. There is only minor misalignment sensitivity given for upward irradiance

components as well as within and below a cloud layer (Wendisch et al. 2001), provided there is no direct shortwave downward component, i.e., we have an optical thick cloud (opacus). To determine the observed horizon, the three Eulerian angles need to be measured. In our setup, the roll and pitch angles were obtained with a two-axis inclinometer AIT700 based on MEMS technology, fabricated by Althen Mess-und Sensortechnik GmbH, Germany. It can be operated over a wide range of ambient temperatures ( $-25$  to  $+85$  °C) and was mounted on the CMP22 pyranometer pair (Fig. 1). The inclinometer uncertainty comprises cross-axis sensitivity and two temperature-dependent components: a thermal zero shift and a thermal sensitivity shift. Given an ambient temperature of  $-8$  °C—which is a good measure for the observations discussed here—it sums up to an uncertainty of 1.5%. It is mandatory to include the error analysis in case of direct sun, too.

The third required angle (yaw) was determined as the difference between wind—measured by the wind vane—and the apparent azimuth of the sun (calculated). To account for the tilt correction, the analytical approach described by Bannehr and Schwiesow (1993) and Saunders et al. (1992) has been applied here. The wind vane with the sensor payload was less affected by fast changes in the wind vector due to its higher inertness compared with the unpacked vane.

### 2.3 Radiative flux calculations

The net radiation  $F_{\text{net},i}$  is defined as the difference of downward and upward fluxes; thus, for the net flux at atmospheric level, it follows:

$$F_{\text{net},i} = F_{\text{sol},i}^{\downarrow} - F_{\text{sol},i}^{\uparrow} + F_{\text{terr},i}^{\downarrow} - F_{\text{terr},i}^{\uparrow} \quad (1)$$

where  $F_{\text{sol},i}^{\downarrow}$  is the downward shortwave (solar) irradiance, comprising direct and diffuse radiation at level  $i$ ,  $F_{\text{sol},i}^{\uparrow}$  the upward shortwave irradiance,  $F_{\text{terr},i}^{\downarrow}$  the longwave (terrestrial) irradiance emitted by the atmosphere, and  $F_{\text{terr},i}^{\uparrow}$  the upward longwave irradiance stemming from surface and atmospheric column under investigation. Considering the uncertainty, all relevant effects (calibration uncertainty, temperature dependence of sensitivity, non-linearity error, spectral sensitivity/selectivity, tilt response, directional error, zero offsets, calculation of tilting angles) of the various measured components are taken into account (see Table 1 for details). We estimate a total uncertainty of 10.2% for the net radiation and 5.48% for the albedo. For a pyranometer tilted from the horizontal plane, Saunders et al. (1992) propose to correct the measured downward shortwave irradiance according to:

$$F_{\text{sol},i,c}^{\downarrow} = \frac{F_{\text{sol},i}^{\downarrow}}{1 - f(\theta) \left( 1 - \frac{\cos\beta}{\cos\theta} \right)} \quad (2)$$

where  $F_{\text{sol},i,c}^{\downarrow}$  is the corrected downward shortwave irradiance and  $f(\theta)$  is the fraction of the direct component in the shortwave downward flux (ranging from 0 to 1, obtained by clear-sky radiative transfer simulations). The angle of incidence  $\beta$  is calculated using:

$$\cos\beta = -\cos R \sin P \sin\theta \cos(H-A) - \sin R \sin\theta \sin(H-A) + \cos R \cos P \cos\theta \quad (3)$$

where  $R$  is the roll angle,  $P$  the pitch angle,  $\theta$  the sun zenith angle,  $H$  the heading angle, and  $A$  the solar azimuth angle.

To get the net longwave irradiance  $F_{\text{net, terr, } i}$ :

$$F_{\text{net,terr},i} = F_{\text{terr},i}^{\downarrow} - F_{\text{terr},i}^{\uparrow} \tag{4}$$

Heating rate computations are performed based on a vertical resolution of 100 m. To calculate the radiative heating/cooling rates (HR) at level  $i$ , we use:

$$\text{HR}_i = \frac{1}{c_p * \rho(z_i)} \frac{\delta F_{\text{net},i}}{\delta z_i} \tag{5}$$

where  $c_p$  is the specific heat capacity of air,  $\rho(z_i)$  the air density, being a function of altitude  $z_i$ , and  $\frac{\delta F_{\text{net},i}}{\delta z_i}$  the change of the net radiative flux with altitude. The uncertainty of the retrieved heating rate is estimated as 14.42%.

Analogously, a longwave heating rate is calculated taking into account the longwave net radiative flux divergence . only. For simulation of fluxes, the radiative transfer package *Streamer* (Key and Schweiger 1998) was applied that allows to simulate broadband fluxes for a wide variety of atmospheric states. Within *Streamer*, a large number of cloud ice particle models and surface characteristics are provided. In our study, we constrain the atmospheric state in the model by the following measurements:

- Profiles of air temperature, humidity, and pressure: tethered balloon-based soundings up to the maximum heights 1.575 km and 1.975 km (sensor quality linked to high-precision observations at the boundary layer site Falkenberg near Meteorological Observatory Lindenberg) and daily routine radiosoundings (standard launch time 11 UTC)
- Aerosol optical depth (AOD) at 600 nm: local readings from SP1A sun photometers

**Table 1** Uncertainty budget for solar and terrestrial irradiance observations, single component contributions, according to manufacturer specifications

Characteristics Instrument	CMP22	CGR4
Calibration uncertainty	2%	3%
Temperature dependence of sensitivity (-20... +50 °C)	0.5%	< 1%
Non-linearity error	0.2%	< 1%
Spectral sensitivity/selectivity	2%	< 5%
Tilt response	0.25%	1%
Directional error	5 Wm <sup>-2</sup> @ 1000 Wm <sup>-2</sup> , 0.5%	Not defined
Zero offset	A 3 Wm <sup>-2</sup> B 1 Wm <sup>-2</sup> total 4 Wm <sup>-2</sup> , corresponding to 1% @ 400 Wm <sup>-2</sup>	A: not defined B: < 2Wm <sup>-2</sup> , plus window heating effect < 4 Wm <sup>-2</sup> , total 6 Wm <sup>-2</sup> @ 240 Wm <sup>-2</sup> corresponding to 2.5%
Tilting angles	1.5%	1.5%
Total uncertainty irradiance	2.81% downward, 2.76% upward (directional error = 0)	6.74%

- Ozone: column amount from the ozone monitoring instrument (OMI), available at <https://aura.gsfc.nasa.gov>. Even local sun photometer evaluations at AWI station Ny-Ålesund are using satellite-based ozone amount
- Surface temperature,  $T_{\text{surf}}$ : a surface temperature—essential for the calculation of longwave upward radiation—was not available close to observation site and therefore needed to be calculated from BSRN measurement of longwave upward radiation readings at 1.30 m aboveground using:

$$T_{\text{surf}} = \sqrt[4]{\frac{F_{\text{terr},s}^{\uparrow}}{\varepsilon_{\text{surf}} \sigma}} \quad (6)$$

where  $F_{\text{terr},s}^{\uparrow}$  is longwave upward radiation measured close to ground, and  $\varepsilon_{\text{surf}}$  is the surface emissivity and  $\sigma$  the Stefan-Boltzmann constant.

- Surface emissivity of snow with respect to age and estimated grain size of snow cover is set according to the findings of Hori et al. (2006)
- Cloud base height from ceilometer (Maturilli 2016)

Temperature at the cloud base is given by the tether sounding itself. Geometrical cloud thickness is detected in the radiation data for the cases when the sounding passed through a cloud layer. Concerning the microphysical parametrization of the clouds—liquid-water content and effective radii of the droplets—mean summertime Arctic clouds characteristics according to the review in Curry and Ebert (1992) are assumed.

Several technical aspects contribute to the overall measurement uncertainty of irradiances. All relevant numbers are listed in Table 1, separated into solar and terrestrial observations performed with the specified instrumentation. To get the total uncertainty of the irradiance, the square root of the sum of the squared single uncertainty contributions is calculated (Cook 2002), analogous to get the uncertainty of albedo, net radiation, and heating rate.

## 3 Observations

### 3.1 Site characteristics of Ny-Ålesund (78.9° N; 11.9° E)

Ny-Ålesund is an international research community located at the Kongsfjorden on the west coast of Svalbard (Spitsbergen). Here, the Alfred Wegener Institute operates a variety of atmospheric measurements including basic surface meteorology (Maturilli et al. 2013), daily radiosoundings (Maturilli and Kayser 2016), weekly ozone soundings, AOD retrieval using sun photometer, and radiation measurements contributing to the BSRN (Maturilli et al. 2015). Campaign-operated soundings using tethered balloons as a carrier at Ny-Ålesund are restricted in timing by air traffic requirements and are generally limited to a maximum height of 2 km aboveground. The tethered balloon campaign in May 2015 was core part of the project “Vertical profile of the net radiation balance” with the aim of characterizing clear-sky profiles of net radiation as well as to get a snapshot of the radiative flux profile under typical Arctic boundary layer cloud conditions. All measurements were conducted during polar day conditions. Figure 2 provides a bird’s eye view of the location. The distance from observatory to



**Fig. 2** Ny-Ålesund and the surroundings, seen from 1300 m aboveground on May 13, 2015. The sonde is fixed at the tether line 3 m below the camera. The center of the red circle marks the location of the balloon hall, associated to the observatory, being the starting point of the soundings

coastline is only 300 to 500 m in all northerly directions. About 1 km south of the village, the slope of Mount Zeppelin (474 m) starts to rise.

Vertical soundings by tethered balloon take up to about 30 min for a profile reaching 2000 m aboveground. Therefore, atmospheric (radiative) stationarity is required during the recording of a profile. Consequently, shortwave flux profiles for the investigation of albedo are rejected in case of changing cloudiness.

### 3.2 Albedo

In Ny-Ålesund, the surface-based solar upward flux instrumentation has the predominantly snow-covered surface in its downward-looking hemispherical view. From the higher elevations of the tethered balloon platform, the observed terrain is getting more complex. The enlarged hemispherical view includes some infrastructure of the village (houses, roads), the dark surface of the open fjord water, and effects of the inclined surface of the mountains. Largely different aerosol loads may have impact on albedo comparison. During the clear-sky soundings on May 07, 08, and 13, 2015, the sun photometer observed aerosol optical depth at 500 nm of 0.095, 0.063, and 0.076 on average. We would not expect to see these rather small discrepancies in broadband radiometry. The measured shortwave upward flux profiles are provided in Fig. 3, being strongly modulated by the solar zenith angle, so the highest values are observed around noon. The profiles taken under overcast conditions show no clear dependence on the solar zenith angle due to the impact of varying cloud optical thickness.

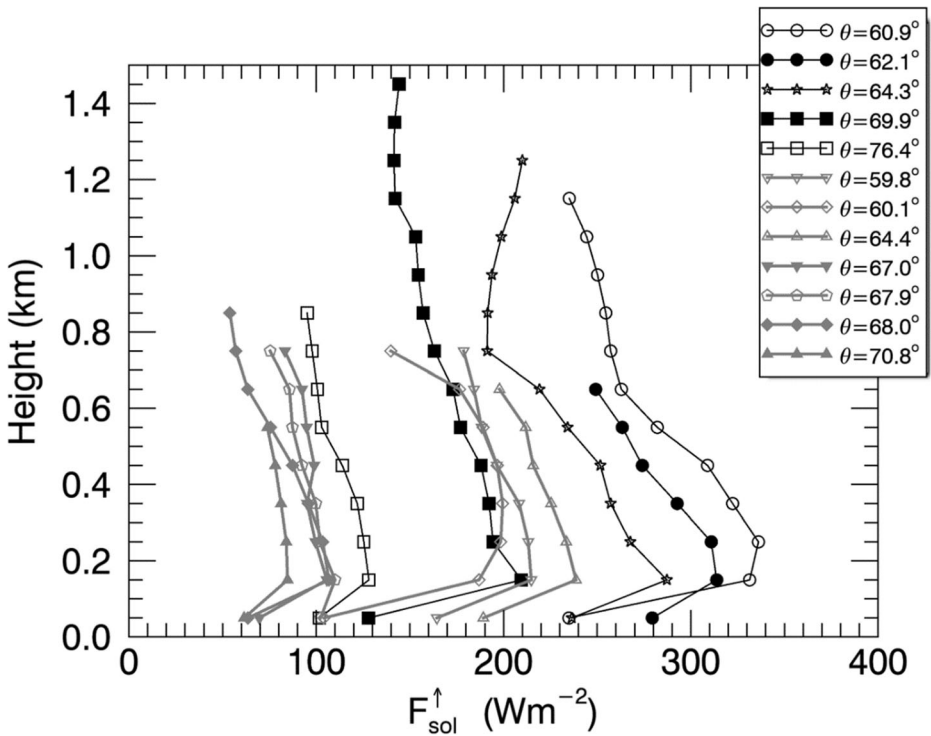


**Fig. 3** Profiles of shortwave upward fluxes above Ny-Ålesund taken under clear-sky conditions (black curves) and under overcast conditions (gray). Top of the overcast profiles is 50 to 100 m below the cloud base

The profiles of albedo, grouped to “clear sky” (5 profiles) and “overcast” (7 profiles) in Fig. 4 show a maximum at 150 to 250 m a.s.l. ranging from 0.51 to 0.67 with greater values to lower sun elevation in clear-sky conditions. The albedo profiles at overcast conditions tend to show 0.09 to 0.14 higher values at all height levels. For the local conditions in Ny-Ålesund, albedo decreases with height by  $-0.040/100$  m in clear-sky conditions over a range of 150 to 750 m, then remaining constant up to 1150 m above sea level. Sun zenith angle ( $\theta$ ) during clear-sky measurements ranges from  $60.8^\circ$  to  $80.4^\circ$  over all profiles. In overcast conditions, an albedo decrease rate of  $-0.034/100$  m is observed (from 150 to 750 m a.s.l.). Generally, similar characteristics of the profiles are found in all soundings: a strong gradient close to ground leads to the maximum albedo values at 150 to 250 m followed by decreasing values with height. Figure 2 illustrates the local surface conditions that explain the height dependence of the albedo profiles. With the growing footprint of the downward-looking sensor during ascent, the fraction of bright snow-covered surface increases to the point when the dark fjord water surface enters the footprint, leading to the decreasing albedo values once the sensor is above 150 to 250 m height. Shortwave upward radiative flux is describing the surface property and the atmospheric layer between surface and sensor, whereas the incoming flux contributes to normalize the result.

Clear-sky soundings at fixed altitudes over several hours—almost undisturbed by clouds—were performed on May 08 (cirrus clouds at 6 to 7 km base height at 15:00, 19:30, and 20:45 UTC according to ceilometer record) and on May 13, 2015 (sudden end at 18:40 UTC due to a stratus cloud deck based at 600 m). The continuous sounding in fixed altitude was chosen to

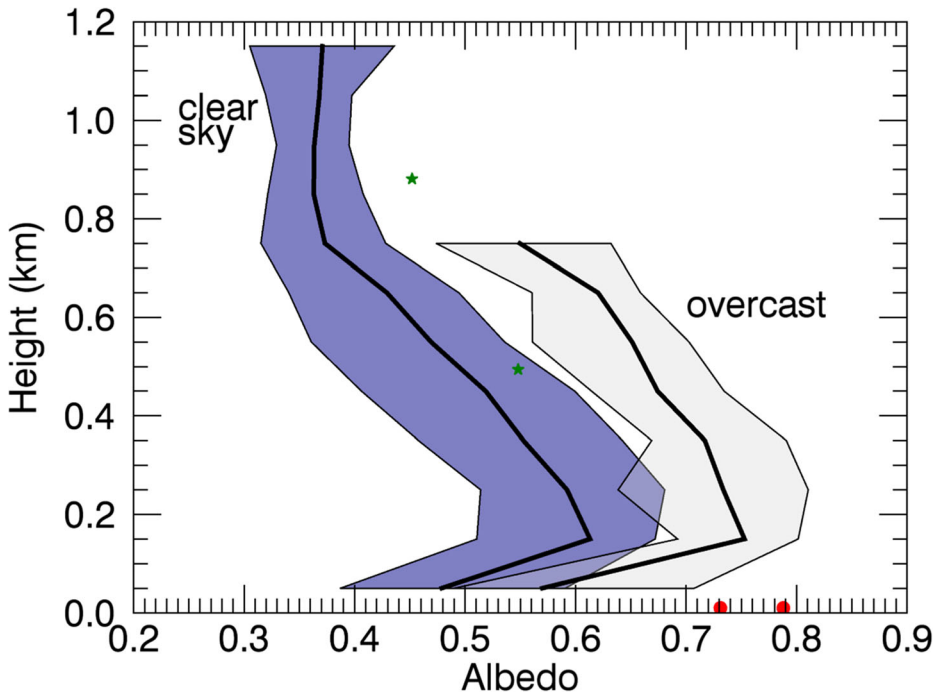


**Fig. 4** Averaged profiles of albedo and minimum-maximum range, separated into the categories clear-sky (blue) and overcast (light gray). Green stars show the means of time series (discussed in section 3.2), red circles the corresponding near-surface readings at the BSRN field

proof the stability of the results and test the influence of the wind speed. The means and standard deviations of pitch and roll angles were  $(-5.8^\circ \pm 1.7^\circ, 4.2^\circ \pm 1.5^\circ)$  on May 08, 2015 and  $(-3.9^\circ \pm 0.7^\circ, -1.8^\circ \pm 0.5^\circ)$  on May 13, 2015.

The meteorological conditions in the local boundary layer at dedicated observation levels were quite similar on both days (Figs. 5 and 6). The temperature was almost constant at about  $-7^\circ\text{C}$  on May 08 (at 881 m a.s.l.) and about  $-8^\circ\text{C}$  on May 13 (at 494 m a.s.l.). Relative humidity was almost constant at about 51% on May 08 but showed an increase from 50 to 75% on May 13. Both situations were characterized by a weak east-southeasterly wind at sounding level with wind speed decreasing from 4 to  $3\text{ ms}^{-1}$  on May 8 while on May 13 measurements started at even a lower wind speed of  $2\text{ ms}^{-1}$  calming further during the sounding. The corresponding time series of the albedo are given in Fig. 7. On May 8, the albedo resulted in  $0.452 \pm 0.090$ , whereas  $0.548 \pm 0.034$  was observed 5 days later. However, the temporarily matching surface-based observations varied only slightly and show a remarkably higher absolute level: the averaged albedos at the BSRN field were  $0.788 \pm 0.017$  and  $0.731 \pm 0.014$ , respectively. The large discrepancies between near-surface and lifted observations were caused by the different sensor footprints explained above. Furthermore, ideally, a tethered balloon would have lifted the sonde vertically with the perpendicular above the winch. In reality, horizontal displacement occurs even for streamlined balloons due to wind speed and free buoyancy. In our case study, the wind direction was similar on both days, but wind speed was on average twice as much on May 8 ( $2.6\text{ ms}^{-1}$ ) compared with that on May 13 ( $0.8\text{ ms}^{-1}$ ), respectively. There is no GNSS information on the exact location of the sensor available; thus, altitude is calculated using air pressure readings. Therefore, we assume a horizontal drift of

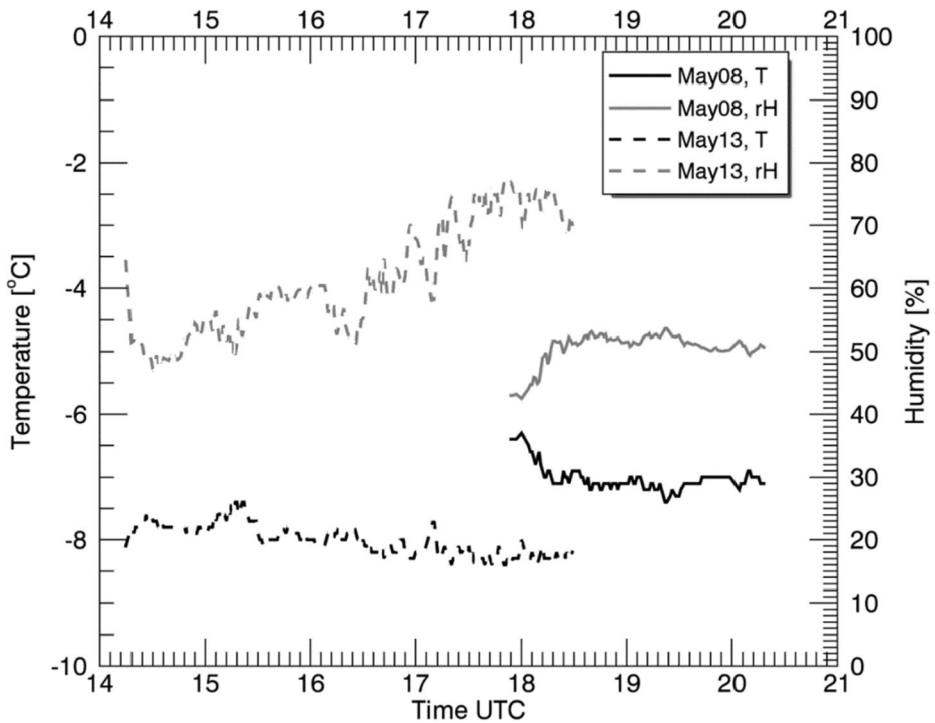


**Fig. 5** Time series of temperature and relative humidity on May 08, 2015, at 881.6 m a.s.l. ( $\sigma = 8.5$  m) and on May 13 at 493.9 m ( $\sigma = 4.4$  m), respectively. Standard deviations refer to the geometrical height of the sensor

200 m toward the northwest on May 8. This corresponds to an average attack angle of the rope of about  $75^\circ$ , which is in line with on-site visual observation. Under this assumption, the perpendicular of the sonde on May 08 was situated at the coastline, separating bright, prevailing snow-covered land surface and dark ice-free seawater surface. Hence, the upward shortwave flux within the footprint of the sensor was reflected by snow and to a wider extent by dark sea surface. To quantify the impact of both contributing surface types on the measured albedo, the fractions of snow surface and sea water surface were varied in the radiative transfer calculations, modifying the fraction in steps of 10%. Selecting a fraction of 50% for both, we get an albedo of 0.443 to 0.507 at 881 m (May 8) above sea level, covering a range of sun zenith angle from  $73.6^\circ$  to  $82.05^\circ$ . This corresponds very well to the observations ( $0.452 \pm 0.090$ ). If the coastline was a straight line, these results would imply land surface fractions of half snow-covered land, half dark seawater. For the launch time on May 13, an albedo of 0.399 is simulated (900 m a.s.l.,  $\theta = 64.3^\circ$ ), which is well below the measured value. However, a modification of surface fractions to a composite of 70% snow and 30% seawater leads to an albedo of 0.526 to 0.581 during the measurement period (measured average, 0.548). The model calculations suggest that due to the horizontal drifting of balloon and sonde on May 8, the fraction of snow-covered area in the field-of-view of the sensor was reduced from 70 to 50%. Besides the balloon drift, the continuous measurement set up at fixed altitude delivered stable results. There was a higher standard deviation in albedo with stronger winds of up to  $4 \text{ ms}^{-1}$ —almost factor 3 compared with weak wind conditions, likely related to the sensor location vertically above the coastline with its strong gradients in shortwave upward radiation.

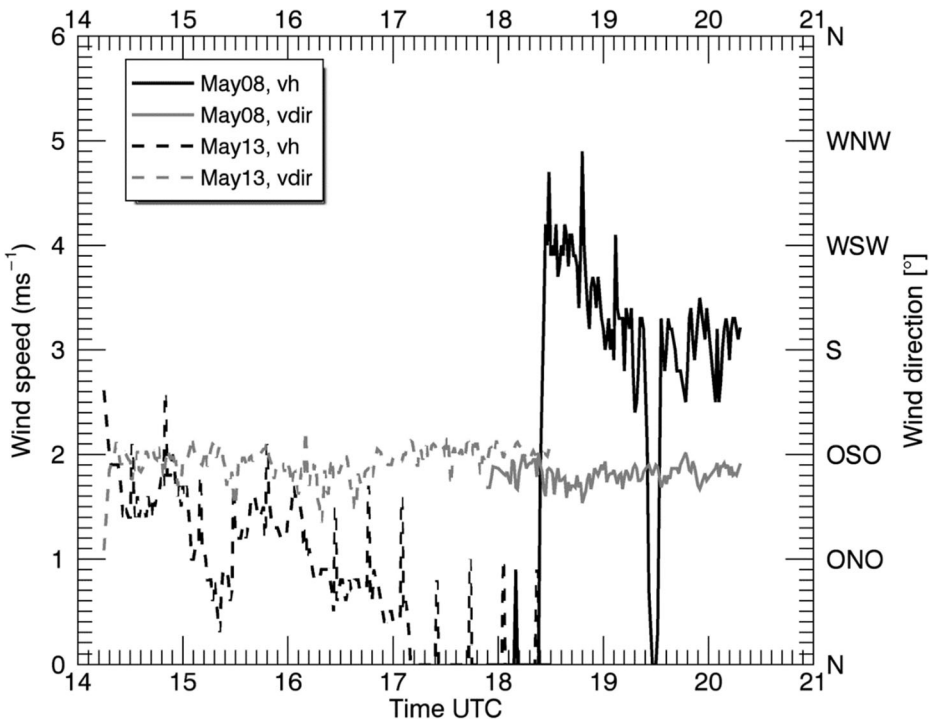


**Fig. 6** Time series of wind velocity and direction on May 08, 2015, at 881.6 m a.s.l. ( $\sigma = 8.5$  m) and on May 13 at 493.9 m ( $\sigma = 4.4$  m), respectively. Standard deviations refer to the geometrical height of the sensor

### 3.3 Radiative fluxes under clear-sky and cloudy conditions

Atmospheric longwave downward radiation usually shows a well-defined decrease with increasing height in a well-mixed boundary layer due to the adiabatic temperature gradient. Exceptions in case of thermal inversions are a common feature in the Arctic. During the tethered balloon campaign in Ny-Ålesund, a thermal inversion was observed on May 13 at 12:39 UTC (Fig. 8). Here, a thermal inversion layer at 750 m a.s.l. was detected, evident in the profile of potential temperature above 750 m. The radiative effect results in an increase of longwave downward radiation of  $7.4 \text{ Wm}^{-2}$  between 650 and 750 m. It corresponds to an increase of longwave upward radiation of  $6.0 \text{ Wm}^{-2}$  at the same level. Due to its almost counterbalancing net effect, the thermal inversion cannot be detected in the net longwave radiation profiles. Still, the importance of thermal inversion layers for longwave downward radiative heating within the atmospheric column and its potential contribution to the bottom-amplified warming of the Arctic atmosphere need to be considered.

Low-level clouds are a worthwhile subject of investigation with tethered balloon-borne equipment. Limited by the technical restrictions of the equipment plus administrative restrictions by the flight authority, we aimed for the detection of stratus or stratocumulus clouds with cloud base height between 500 and 1300 m and a vertical thickness of 500 m maximum. These types of clouds frequently occur in the Arctic region (Tsay et al. 1989; Nomokonova et al. 2018). Generally, riming of the sensors may severely affect radiative flux measurements in liquid-water clouds, and all readings taken afterwards. Ice cover on the radiometer domes accumulates

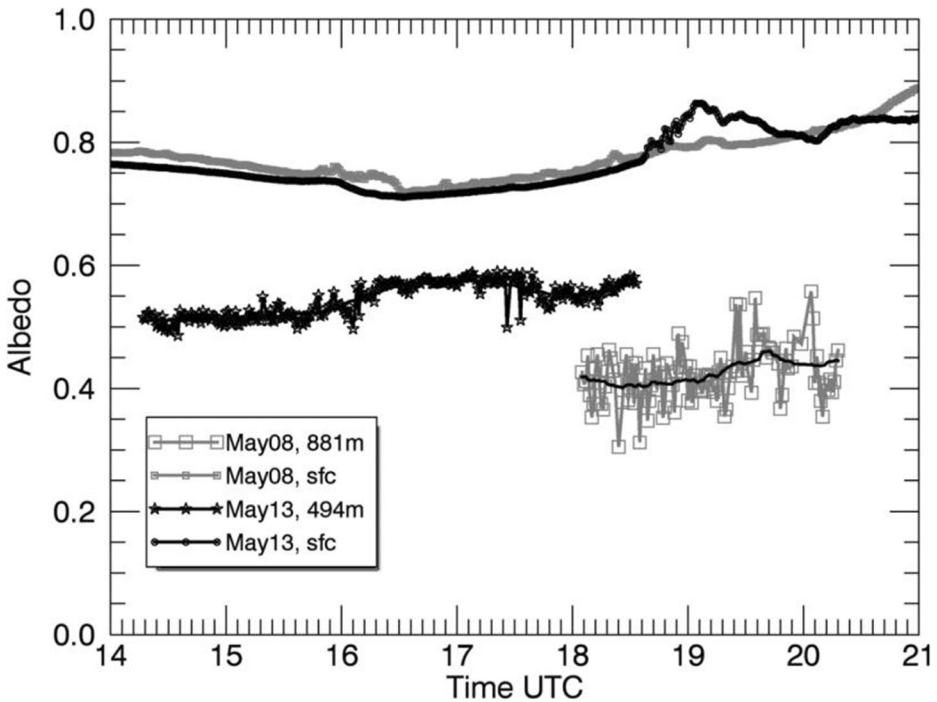


**Fig. 7** Clear-sky albedo time series on May 08, 2015, at 881.6 m a.s.l. ( $\sigma = 8.5$  m) and on May 13 at 493.9 m ( $\sigma = 4.4$  m) versus near-surface readings

and persists if temperature is below frost point during sounding, ambient air is close to saturation, and the sensor is not exposed to sunlight. In that case, riming can be detected even after the descent when the sensor is back on the ground. We never observed riming and thus exclude related effects for the discussed cloud profiles. On two days (May 11 and 12, 2015), tethered flights through stratus clouds were performed. A total of 4 consecutive profiles taken on May 12 are discussed here, describing the transition phase from overcast to partly cloudy conditions.

### 3.4 The cloudy case study on May 12, 2015

From 11:30 a.m. to 3 p.m., the BSRN station readings of shortwave downward radiative flux show a moderate variability in the signal even though the sky remains overcast all the time. During recording of the first two profiles, solar downward is ranging only from 265 to 288  $\text{Wm}^{-2}$ . When starting the 3rd profile, there are already 305  $\text{Wm}^{-2}$  reached, increasing further to 370  $\text{Wm}^{-2}$  (see Fig. 9). Direct normal solar radiation is at several times higher than 0, but below 20  $\text{Wm}^{-2}$  in the sounding windows. The subsequent decrease of solar downward flux at the end of profile 3 and covering the whole profile 4 time is a consequence of the advection of yet another cloud layer based at 500 m. Terrestrial downward radiative flux (Fig. 9) remains at 283–284  $\text{Wm}^{-2}$  during profiles 1 and 2 and gets more variable within the range 280 to 285  $\text{Wm}^{-2}$  later on. Therefore, a certain part of variability in vertical levels is due to variability in time, most impacting late profile and solar fluxes. The observation of evolution of the lower atmosphere was aborted due to the advection of the lower cloud layer (see ceilometer readings in Fig. 10; Maturilli 2016).

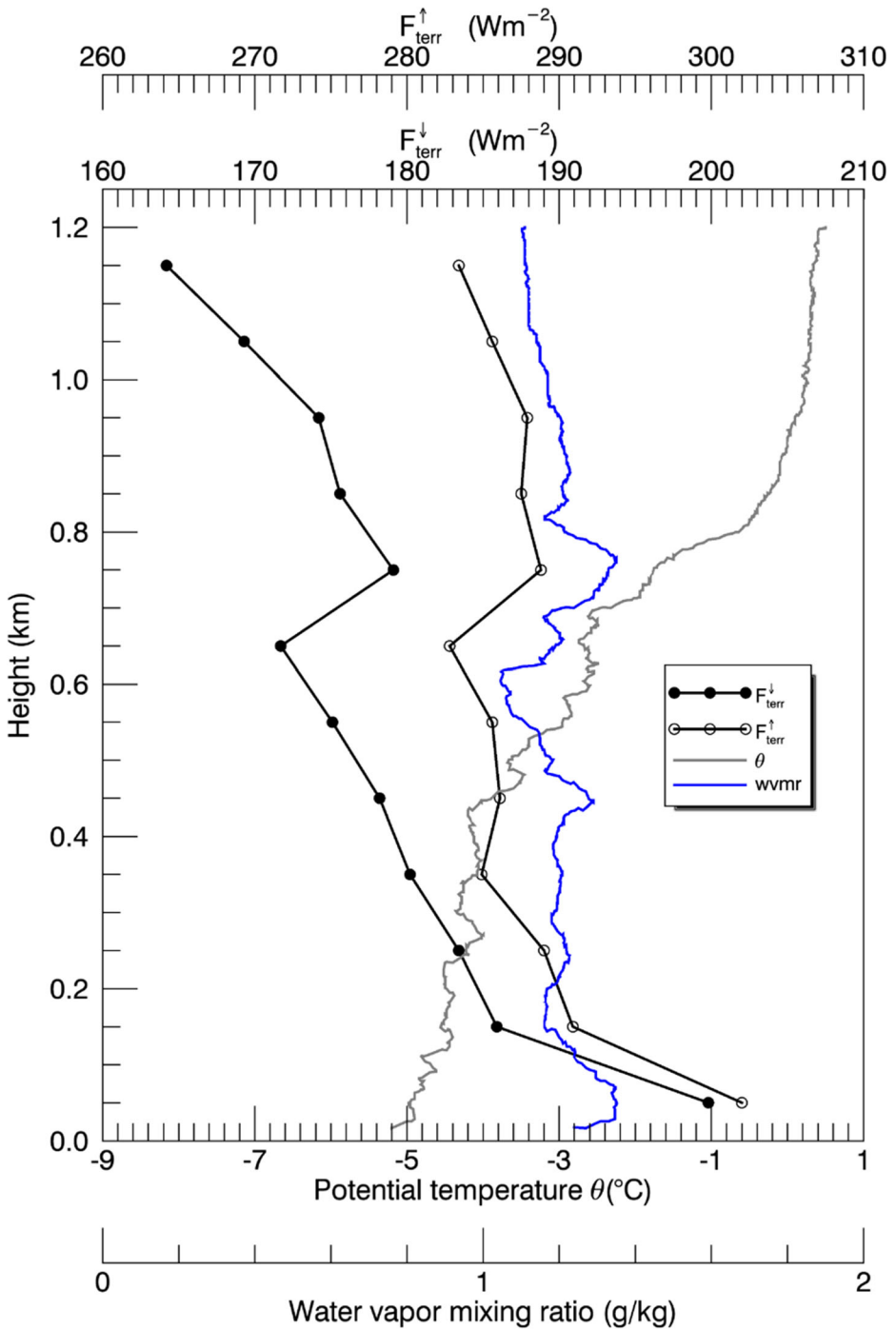


Fig. 8 Clear sky profile of longwave up- and downward radiative fluxes, potential temperature, and water vapor mixing ratio taken on May 13, 2015, 12:39 UTC, above Ny-Ålesund

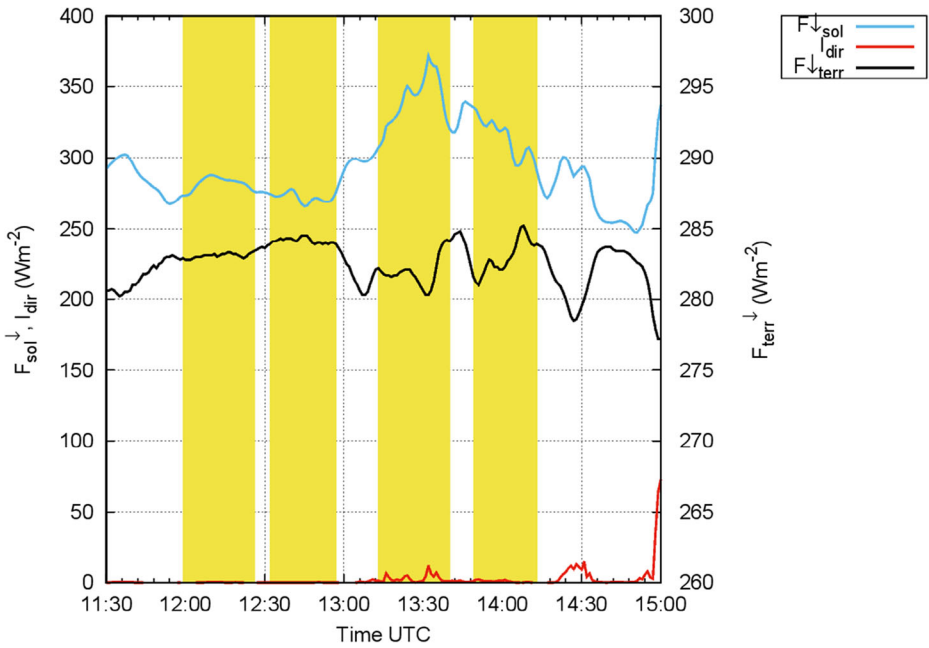


Fig. 9 BSRN near-surface readings of solar and terrestrial downward fluxes during recording of cloud profiles

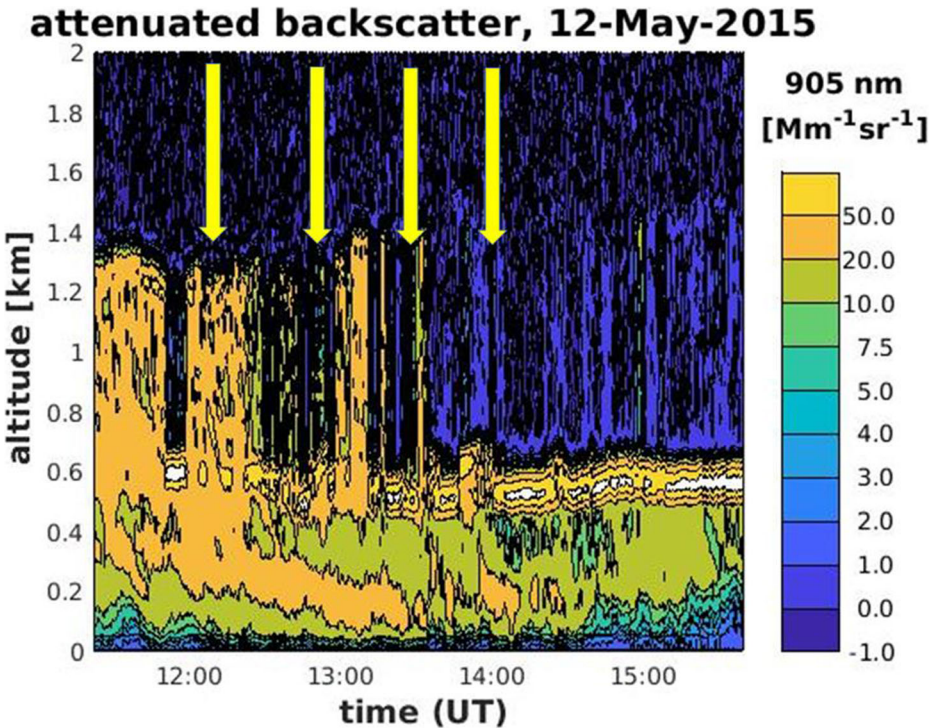


Fig. 10 Time-height cross section of ceilometer-based backscatter during recording of cloud profiles

Temperature at the cloud base is identified from the in situ radiosounding at the respective height. A local temperature minimum was detected at 1486 m ( $-14\text{ }^{\circ}\text{C}$ ). The atmospheric layer between about 1500 and 1600 m was 2 K warmer, and the measured lapse rate above was weaker than below the cloud (Fig. 11). Regarding humidity, a well-mixed boundary layer with relative humidity between 60 and 80% was found below the clouds, and distinctively drier air above the clouds. The wind profile indicated only weak shear in velocity with 4 to 5  $\text{ms}^{-1}$  at cloud level and 1 to 2  $\text{ms}^{-1}$  from southeast both in the boundary layer and above the dissolving cloud layer.

## 4 Discussion

### 4.1 Flux and heating rate profiles

To get the height of the cloud top gradients of temperature, relative humidity, and downward solar and downward terrestrial radiative fluxes are under investigation. In comparison with the profiles observed earlier in the day, the gradient is less sharp in temperature and shows a step structure in humidity—even in all cases dropping down to 20%—with the 13:30 and 14:00 flights. It is interpreted as having observed a less plane and more structured cloud top with variability in top height—depending on where exactly probing is done. Taking into account that cloud layer is moving in the meantime, the irradiance field is changing during observation. Nevertheless, a gradient-based approach for the detection of cloud top height works very well with thermodynamic and radiative profiles (see Table 2 for results).

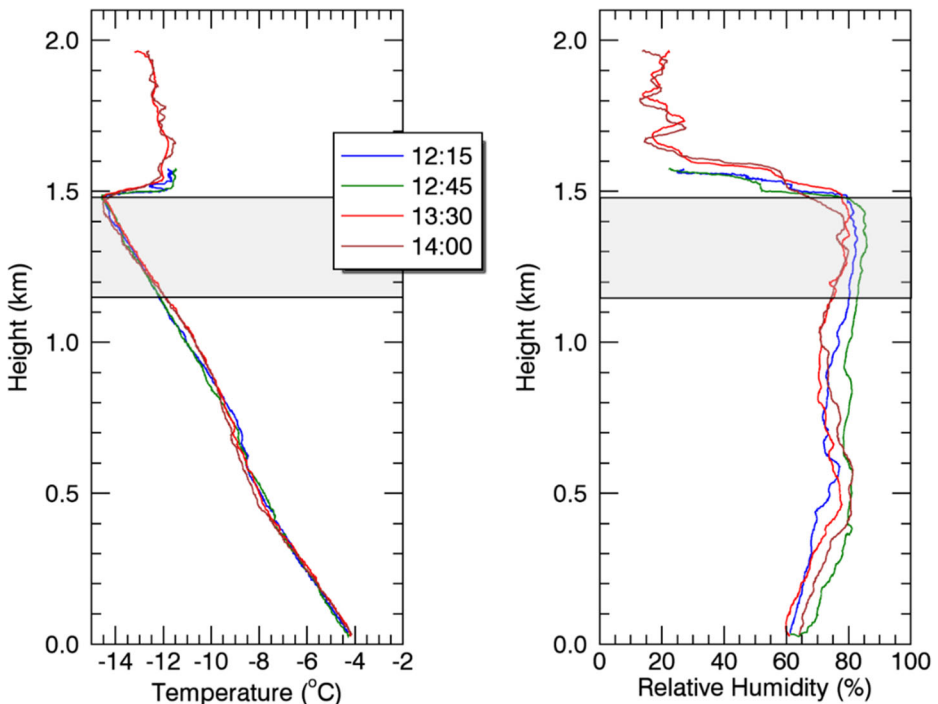


Fig. 11 Profiles of temperature and humidity recorded during 4 cloud flights on May 12, 2015, at Ny-Ålesund

**Table 2** Determined height of cloud top (m) from gradient approaches using temperature, relative humidity, downward solar and downward terrestrial radiative flux

Time	Parameter			
	$T$	rH	$F_{\text{sol}}^{\downarrow}$	$F_{\text{terr}}^{\downarrow}$
12:15	1486	1488	1454	1488
12:45	1493	1481	1446	1446
13:30	1496	1501	1466	1466
14:00	1480	1423	1304	1465

The most stable results are provided by the temperature gradient approach: all cloud top heights do vary in a vertical range from 1480 to 1496 m. The humidity-based results are quite the same except for the last profile suggesting a cloud top at 57 m lower than with temperature gradient. Cloud tops from radiative fluxes tend to be from comparable ( $F_{\text{terr}}^{\downarrow}$  at 12:15 and 14:00 UTC) to slight underestimations up 47 m. An apparent mismatch of 176 m is found with solar downward at 14:00 UTC.

Solar fluxes showed a distinct increase of about  $200 \text{ Wm}^{-2}$  when passing the cloud layer during ascent. Longwave downward radiation dropped down to 130 to  $140 \text{ Wm}^{-2}$  above the cloud, representing the cloud free troposphere. In contrast, the drop of the longwave upward component is only about half (Fig. 12).

Most of the variability in the net flux divergence for the cloudy case originated from the shortwave downward radiation, here composed of two effects: the increase in insolation when passing the cloud from below, and the observation of varying solar flux below the cloud due to inhomogeneity in the cloud deck. The latter has been identified as artificial: different observation times refer to different locations relative to the patchy cloud deck. The profile of shortwave upward radiation peaked just above the cloud top.

Terrestrial downward flux was decreasing rapidly with maximum rates of  $-2 \text{ Wm}^{-2}/\text{m}$  when passing the cloud top from below. With progressing time, the vertical gradients for solar upward and terrestrial downward flux decreased due to the continued decrease in the cloud fraction. The gradient of the terrestrial upward flux was always below  $0.5 \text{ Wm}^{-2}/\text{m}$ . In the albedo profile, the transition through the cloud was less sharply pronounced. We observed an increase from 0.62 to 0.72 below the cloud (except near-surface feature mentioned earlier in this text) to 0.72 to 0.80 above. Freese and Kottmeier (1998) reported an almost constant difference between up- and downward shortwave radiative flux densities occurring with absolute fluxes less than  $50 \text{ Wm}^{-2}$  due to very low sun zenith angles. Here, we observed a different behavior: almost constant to slightly increasing difference due to increasing downwelling shortwave radiative flux below and in the cloud and a shortwave net excess of about  $40 \text{ Wm}^{-2}$  at the cloud top ( $60.8^\circ < \theta < 62.5^\circ$ ).

The total net radiative effect above the cloud top is distinctly negative ( $-50 \text{ Wm}^{-2}$ ) due to a sharp negative gradient in longwave downward radiation while longwave upward radiation only slightly decreases. Local heating or cooling is driven by the net flux divergence and thus by the vertical gradient of the net radiation. The corresponding radiative heating rates are shown in Fig. 13. For the last profile at around 14:00 UT on May 12, the heating rate is left out intentionally due to changes in cloudiness during the profiling. At all other observation times, a radiative cooling at the cloud top with rates from  $-40.4$  to  $-62.1 \text{ Kd}^{-1}$  is observed, with

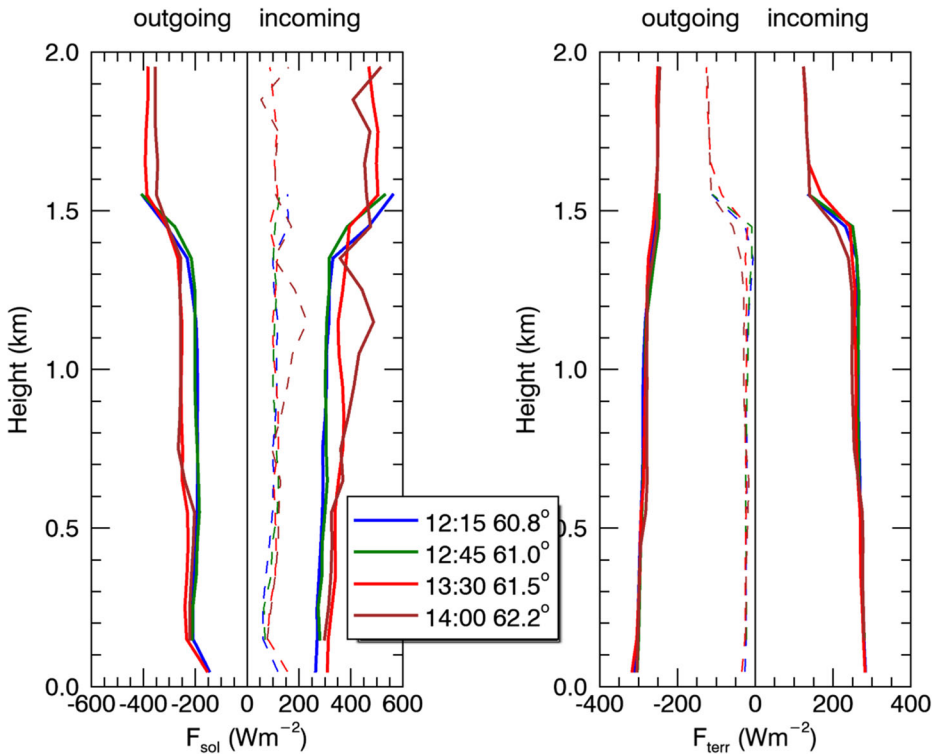


**Fig. 12** Radiative flux profiles recorded during 4 cloud flights on May 12, 2015, at Ny-Ålesund, separated by shortwave and longwave contributions. Net radiation is plotted in dashed lines

implications for the thermal inversion observed in the height range of 1490–1600 m with a temperature increase of 2 to 2.5 K.

## 4.2 Model comparison

Observed cloud characteristics as far as they are used for the model comparison are provided in Table 3. We take the simulations, driven using observations (cloud geometrical parameters, profiles of temperature and humidity, AOD, ozone content) and reasonable assumptions, as a plausibility check for the observational data. For 14:00 UTC, only longwave fluxes can be employed. Temperature at cloud base is obtained from the radiosounding at that height. Thickness of the cloud layer is derived using the additionally inferred cloud top height. It is identified by the temperature lapse rate becoming positive, i.e., the temperature inversion base. This level coincides very well to the lapse in relative humidity except for the profile around 14:00 UTC: here, the cloud top is detected 57 m lower than that in the precursor profiles (see Table 2). Due to the lack of observations of microphysical cloud parameters—the local cloud radar has started operation recently—we have to refer to former studies on low-level Arctic clouds as input to the radiative transfer model study. The assumption of a liquid water cloud might not be fulfilled here, even though several aspects support that. The midnight sun has started 4 weeks ago in mid-April; thus, there is permanent insolation. A study based on 13 months of Ny-Ålesund cloud radar data revealed the highest probability of occurrence of mixed-phase clouds in May 2017 as well as a decrease of ice clouds and an increase of

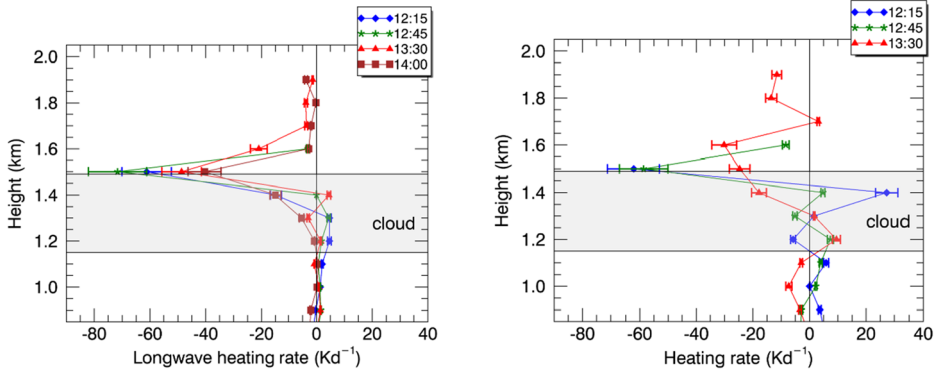


**Fig. 13** Profiles of heating rates retrieved for cloud flights on May 12, 2015. Numbers for cloud base (1.15 km) and cloud top height (1.49 km) represent conditions during recording of the first three profiles

liquid clouds in comparison with the previous winter months (Nomokonova et al. 2018). Ebell et al. (2020) reported recently that monthly mean frequency of occurrence of liquid-water paths  $> 5 \text{ gm}^{-2}$  in May is almost on the level of summer months, whereas the occurrence of ice-water paths  $> 0$  is significantly lower with respect to the winter months. To describe the cloud microphysics, the parameters cloud optical depth  $\tau$  (the path integral over the absorption coefficient) and the cloud droplet effective radius  $r_e$  will be used (Hansen and Travis 1974). According to Curry and Ebert (1992) and Freese and Kottmeier (1998), several preset values for  $\tau \in \{2, 5, 10, 15\}$  and  $r_{\text{eff}} \in \{10, 15\}$  were selected. The content of liquid water therefore varies between  $0.039$  ( $\tau = 2$ ,  $r_{\text{eff}} = 10 \text{ }\mu\text{m}$ ) and  $0.438 \text{ g m}^{-3}$  ( $\tau = 15$ ,  $r_{\text{eff}} = 15 \text{ }\mu\text{m}$ ). That set of model parameters producing heating rates closest to the observed is assumed to be close to reality. Table 3 provides an overview of observed and simulated heating rates at cloud base and cloud top.

For the comparison of observed and simulated data, we set a focus on cloud base and cloud top. Results of the Streamer model indicate clear positive heating rates at the cloud base. For flight 1 around 12:15 UTC, a decrease of  $23 \text{ W m}^{-2}$  in terrestrial upward flux is simulated, while terrestrial downward flux remains almost constant. The model provides similar results for the other flights as well. The simulated total heating rates of almost constantly  $8 \text{ Kd}^{-1}$  for the first three flights, lowered to  $5.0 \text{ Kd}^{-1}$  for the last, are in good correspondence to the measurements, but cannot be seen in the 14:00 UTC profile due to the dissolving cloud layer. The observations reveal a slightly weaker gradient in longwave upward flux and therefore a lower heating rate. In contradiction, the cloud top

**Table 3** Cloud characteristics on May 12, 2015, by observation including estimated uncertainty and simulation. Solar zenith angle only slightly varies from  $60.8^\circ$  when starting the first profile to  $62.5^\circ$  at the end of the last descent. A constant liquid-water content of  $0.195 \text{ gm}^{-3}$  is used for computations

Mean time, UTC	Cloud base (cbh, km)	Temp. at cloud base (K)	Cloud thickness (km)	Heating rate at cloud base, observed ( $\text{Kd}^{-1}$ )	Heating rate at cloud base, calculated ( $\text{Kd}^{-1}$ )	Heating rate at cloud top, observed ( $\text{Kd}^{-1}$ )	Heating rate at cloud top, calculated ( $\text{Kd}^{-1}$ )
12:15	1.15	261.0	0.33	$+ 5.9 \pm 0.4$	+ 8.4	$- 62.1 \pm 9.1$	- 45.5
12:45	1.15	261.0	0.33	$+ 7.4 \pm 0.6$	+ 8.3	$- 58.6 \pm 8.6$	- 45.5
13:30	1.15	261.2	0.34	$+ 10.6 \pm 0.8$	+ 7.8	$- 44.2 \pm 6.4$	- 47.0
14:00	0.93	263.0	0.49	$+ 0.2 \pm 0.1$	+ 5.0	$- 40.4 \pm 5.9$	- 26.8

is much more pronounced in radiation data, both in the model and in the observations. Cloud top was more uniform in the beginning of the observation sequence, implying a potentially better representation in the model. The differences between observed and calculated cooling rates vary from  $-16.6 \text{ Kd}^{-1}$  (12:15 UTC) and  $+2.8 \text{ Kd}^{-1}$  (13:30 UTC), both being ascending profiles, respectively. The ascent at 12:15 UTC gives a cooling rate of  $62.1 \text{ Kd}^{-1}$  ( $45.5 \text{ Kd}^{-1}$  by the model) which is almost fully provided by the longwave flux divergence (Fig. 13). The variability of the radiative heating might be explained by heterogeneities at the cloud top at measurement time. Gerber et al. (2014) discuss a slow response effect of the pyrgeometer CG4 with aircraft measurements when crossing cloud top upwards and downwards. Nevertheless, this effect should be negligible here with vertical motions restricted to  $2$  to  $3 \text{ ms}^{-1}$  by the tethered balloon operation. For 12:15 and 13:30 UTC profiles, a strong increase of solar net radiation can be detected, from  $100$  to  $158 \text{ Wm}^{-2}$  (12:15) and from  $86$  to  $118 \text{ Wm}^{-2}$  (13:30). We assume effects due to cloud morphology like multiple reflection (exceeds solar downward) and partly shading of cloud tops (decreases solar upward). Cloud tops do often have a dedicated 3-dimensional structure, depending on cloud type, which is in contrast to plane-parallel assumption inherent with 1D calculations. This causes effects in the radiation field such as additional exposition due to multiple reflection and side effects caused by cloud towers that could be handled by 3D radiative transfer models.

## 5 Conclusions and outlook

In this study, we present solar and terrestrial radiative flux profile observations in an Arctic environment. We describe the baseline clear-sky vertical radiative flux profiles for the Arctic location of Ny-Ålesund, Svalbard. The role of the footprint size for albedo determination over this complex Arctic fjord environment is quantified, and a first observation of the vertical resolved radiative flux in the presence of clouds could be provided. Vertical profiles of albedo reveal a strong dependence on the height of observation related to the heterogeneous surface within the sensors' field of view. In the mountainous fjord surrounding the Ny-Ålesund site, the dark surface of the open fjord water affected the observations over the snow-covered land surface above  $150 \text{ m}$  height. Above that level, a rate of  $-0.04/100 \text{ m}$  has been derived as typical for the local combination of open sea plus snow-covered land surface in clear-sky conditions. Time series of albedo in fixed heights further demonstrate the relative robustness of net radiation observations using a tethered balloon platform. The measurement setup has also proofed its high potential to observe the longwave radiative effect of thermal inversions under clear-sky conditions and to retrieve the radiative effect of clouds. A sequence of 4 measurements in and above Arctic stratus clouds has revealed a weak warming at cloud base (less than  $10 \text{ Kd}^{-1}$ ) and a stronger cooling at the cloud top  $-40.4$  to  $-62.1 \text{ Kd}^{-1}$ . In future, combinations of similar observations using potentially faster radiation sensors with microphysical cloud in situ measurements are expected to provide further details of irradiance gradients related to low-level clouds at various latitudes. Time series at cloud top level can help quantify the variability in radiative fluxes. Balloon-borne clear-sky observations of albedo have the potential to provide a broader view on land surface characteristics with special attention on linking near-surface measurements and satellite retrievals.

**Acknowledgments** We kindly thank AWI for the opportunity to perform tethered balloon soundings at the AWIPEV research base in Ny-Ålesund, Svalbard, and the local flight authority for supporting our issues. The sounding procedures were strongly supported by Jürgen Graeser, Ingo Beninga, Rene Bürgi, and the AWIPEV station staff. We further thank Christoph Ritter for providing AOD data. Special thanks to technical staff Jörg Karpinsky and Steffen Gross at Meteorological Observatory Lindenberg for adapting the sensors, setting up the

data acquisition, and supporting the improvement of all handling aspects. We highly appreciate the constructive comments and suggestions of the three anonymous reviewers.

**Funding Information** Open Access funding provided by Projekt DEAL.

## Compliance with ethical standards

**Conflict of interest** The authors declare that they have no conflict of interest.

**Open Access** This article is licensed under a Creative Commons Attribution 4.0 International License, which permits use, sharing, adaptation, distribution and reproduction in any medium or format, as long as you give appropriate credit to the original author(s) and the source, provide a link to the Creative Commons licence, and indicate if changes were made. The images or other third party material in this article are included in the article's Creative Commons licence, unless indicated otherwise in a credit line to the material. If material is not included in the article's Creative Commons licence and your intended use is not permitted by statutory regulation or exceeds the permitted use, you will need to obtain permission directly from the copyright holder. To view a copy of this licence, visit <http://creativecommons.org/licenses/by/4.0/>.

## References

- Alzheimer JM, Anderson GA, Whiteman CD (1993) Stabilized platform for tethered balloon soundings of broadband long- and shortwave radiation. Technical report, Pacific northwest laboratory, Richland, Washington 99352. Conference proceedings, 7 p., presented at the 73rd American Meteorological Society (AMS) Annual Meeting, Anaheim, CA, 17–22
- Bannehr L, Schwiesow R (1993) A technique to account for the misalignment of pyranometers installed on aircraft. *J Atmos Ocean Technol* 10:774–777
- Boers R, Mitchell RM, Krummel PB (1998) Correction of aircraft pyranometer measurements for diffuse radiance and alignment errors. *J Geophys Res* 103(D13):16753–16758
- Bucholtz A, Hlavka DL, McGill MJ, Schmidt KS, Pilewskie P, Davis SM, Reid EA, Walker AL (2010) Directly measured heating rates of a tropical subvisible cirrus cloud. *J Geophys Res Atmos* 115. <https://doi.org/10.1029/2009JD013128>
- Cook RR (2002) Assessment of uncertainties of measurement for calibration and testing laboratories, Second edn. National Association of Testing Authorities, Australia. ISBN 0–909307–46–6
- Curry JA, Ebert EE (1992) Annual cycle of radiation fluxes over the arctic ocean: sensitivity to cloud optical properties. *J Clim* 5:1267–1280
- Driemel A, Augustine J, Behrens K, Colle S, Cox C, Cuevas-Agulló E, Denn FM, Duprat T, Fukuda M, Grobe H, Haefelin M, Hodges G, Hyett N, Ijima O, Kallis A, Knap W, Kustov V, Long CN, Longenecker D, Lupi A, Maturilli M, Mimouni M, Ntsangwane L, Ogihara H, Olano X, Olfes M, Omori M, Passamani L, Pereira EB, Schmithüsen H, Schumacher S, Sieger R, Tamlyn J, Vogt R, Vuilleumier L, Xia X, Ohmura A, König-Langlo G (2018) Baseline Surface Radiation Network (BSRN): structure and data description (1992–2017). *Earth Syst Sci Data* 10:1491–1501. <https://doi.org/10.5194/essd-10-1491-2018>
- Dubois P (1961) Technik aerologischer Aufstiege über land. In: Hesse W (ed) *Handbuch der Aerologie*. Akademische Verlagsgesellschaft, Leipzig
- Duda DP, Stephens GL, Cox SK (1991) Microphysical and radiative properties of marine stratocumulus from tethered balloon measurements. *J Appl Climatol* 30:170–186
- Ebell K, Nomokonova T, Maturilli M, Ritter C (2020) Radiative effect of clouds at Ny Ålesund, Svalbard, as inferred by ground-based remote sensing observations. *J Appl Meteor Climatol* 59:3–22
- Freese D, Kottmeier C (1998) Radiation exchange between stratus clouds and polar marine surfaces. *Bound-Layer Meteorol* 87:331–356
- Gerber H, Malinowski SP, Buchholtz A, Thorsen T (2014) Radiative cooling of stratocumulus. 14th Conference on Atmospheric Radiation. American Meteorological Society, Boston, MA, p 9.3 [<https://doi.org/10.13140/2.1.4016.2563>]
- Hansen JE, Travis LD (1974) Light scattering in planetary atmospheres. *Space Sci Rev* 16:572–610
- Hori M, Aoki T, Tanikawa T, Motoyoshi H, Hachikubo A, Sugiura K, Yasunari TJ, Eide H, Storvold R, Nakajima Y, Takahashi F (2006) In-situ measured spectral directional emissivity of snow and ice in the 8–14  $\mu\text{m}$  atmospheric window. *Remote Sens Environ* 100:486–502

- IPCC (2014) In: Core writing team, Pachauri RK, Meyer LA (eds) Climate Change 2014: synthesis report. Contribution of Working Groups I, II and III to the Fifth Assessment Report of the Intergovernmental Panel on Climate Change. IPCC, Geneva, Switzerland 151 pp
- Key J, Schweiger AJ (1998) Tools for atmospheric radiative transfer: streamer and FluxNet. *Comput Geosci* 24(5):443–451
- Kipp & Zonen (2001) Instruction manual CG4 pyrgeometer, version 0304. Technical report, available via [www.kippzonen.com](http://www.kippzonen.com). Accessed 12 May 2020
- Kipp & Zonen (2004) Instruction manual CMP22 pyranometer. Technical report, available via [www.kippzonen.com](http://www.kippzonen.com). Accessed 12 May 2020
- Kräuchi A, Philipona R (2016) Return glider radiosonde for in situ upper-air research measurements. *Atmos Meas Tech* 9:2435–2544. <https://doi.org/10.5194/amt-9-2535-2016>
- Long CN, Buchholtz A, Jonsson H, Schmid B, Vogelmann A, Wood J (2010) A method of correcting for tilt from horizontal in downwelling shortwave irradiance measurements on moving platforms. *Open Atmos J* 4:78–87
- Maturilli M (2016) Expanded measurements from station Ny-Ålesund (2015–05). Alfred Wegener Institute - Research Unit Potsdam, PANGAEA. <https://doi.org/10.1594/PANGAEA.863264>
- Maturilli M, Kayser M (2016) Arctic warming, moisture increase and circulation changes observed in the Ny-Ålesund homogenized radiosonde record. *Theor Appl Climatol* 130:1–17. <https://doi.org/10.1007/s00704-016-1864-0>
- Maturilli M, Herber A, König-Langlo G (2013) Climatology and time series of surface meteorology in Ny-Ålesund, Svalbard. *Earth Syst Sci Data* 5:155–163. <https://doi.org/10.5194/essd-5-155-2013>
- Maturilli M, Herber A, König-Langlo G (2015) Surface radiation climatology for Ny Ålesund, Svalbard (78.9°N), basic observations for trend detection. *Theor Appl Climatol* 120:331–339. <https://doi.org/10.1007/s00704-014-1173-4>
- Nomokonova T, Ebell K, Löhnert U, Maturilli M, Ritter C, O'Connor E (2018) Statistics on clouds and their relation to thermodynamic conditions at Ny-Ålesund using ground-based sensor synergy. *Atmos Chem Phys Discuss*. <https://doi.org/10.5194/acp-2018-1144>
- Norris JR, Allen RJ, Evan AT, Zelinka MD, O'Dell CW, Klein SA (2016) Evidence for climate change in the satellite cloud record. *Nature* 536:72–75. <https://doi.org/10.1038/nature18273>
- Ohmura A, Dutton EG, Forgan B, Froehlich C, Gilgen H, Hegner H, Heimo A, Koenig-Langlo G, McArthur B, Mueller G, Philipona R, Pinker R, Whitlock CH, Dehne K, Wild M (1998) Baseline surface radiation network (BSRN/WCRP): new precision radiometry for climate research. *Bull Am Meteorol Soc* 79:2115–2136
- Philipona R, Kräuchi A, Brocard E (2012) Solar and thermal radiation profiles and radiative forcing measured through the atmosphere. *Geophys Res Lett* 39:L13806
- Ramanathan V, Cess RD, Harrison EF, Minnis P, Barkstrom BR, Ahmad E, Hartmann D (1989) Cloud-radiative forcing and climate: results from the Earth Radiation Budget Experiment. *Science* 243:57–63. <https://doi.org/10.1126/science.243.4887.57>
- Saunders RW, Brogniez G, Buriez JC, Meerkötter R, Wendling P (1992) A comparison of measured and modeled broadband fluxes from aircraft data during the ICE89 field experiment. *J Atmos Ocean Technol* 9:391–406
- Shupe M, Intrieri JM (2004) Cloud radiative forcing of the Arctic surface: the influence of cloud properties, surface albedo, and solar zenith angle. *J Clim* 17:616–628. <https://doi.org/10.1175/2010JAMC2468.1>
- Steenefeld GJ, Wokke MJJ, Groot Zwaafink CD, Pijlman S, Heusinkveld BG, Jacobs AFG, Holtslag AAM (2010) Observations of the radiation divergence in the surface layer and its implication for its parameterization in numerical weather prediction models. *J Geophys Res* 115. <https://doi.org/10.1029/2009JD013074>
- Sun J, Burns SP, Delany AC, Oncley SP, Horst TW, Lenschow DH (2003) Heat balance in the nocturnal boundary layer during cases-99. *J Appl Meteorol* 42:1649–1666
- Trenberth KE, Fasullo JT, Kiehl J (2009) Earth's global energy budget. *Bull Am Meteorol Soc* 90:311–324. <https://doi.org/10.1175/2008BAMS2634.1>
- Tsay SC, Stannnes K, Jayaweera K (1989) Radiative energy budget in the cloudy and hazy arctic. *J Atmos Sci* 46(7):1002–1018
- Turner, D.D., Shupe, M.D., and Zwink, A.B.: Characteristic atmospheric radiative heating rate profiles in arctic clouds as observed at Barrow, Alaska. *J Am Meteorol Soc*. Doi:<https://doi.org/10.1175/JAMC-D-17-0252.1>, 2018
- Webb AR, Kylling A, Wendisch M, Jäkel E (2004) Airborne measurements of ground and cloud spectral albedos under low aerosol loads. *J Geophys Res* 109:D20205. <https://doi.org/10.1029/2004JD004768>
- Wendisch M, Müller D, Schell D, Heintzenberg J (2001) An airborne spectral albedometer with active horizontal stabilization. *J Atmos Ocean Technol* 18:1856–1866
- Wild M (2012) Enlightening global dimming and brightening. *Bull Am Meteorol Soc* 93:27–37. <https://doi.org/10.1175/BAMS-D-11-00074.1>
- WMO 2018 Guide to instruments and methods of observation. Technical report, World Meteorological Organization, No. 8, 2018 edition.